FFI Norwegian Defence Research Establishment

21/00963

FFI-RAPPORT

Modeling underwater explosions: Extending Charles to FIVER

Andreas Nygård Osnes

Modeling underwater explosions: Extending Charles to FIVER

Andreas Nygård Osnes

Norwegian Defence Research Establishment (FFI) 27 September 2021

Keywords
Flerfasestrømning
Eksplosjoner
Sjokkbølger
Fluiddynamikk

FFI report
21/00963

Project number
1447

Electronic ISBN
978-82-464-3344-8

Approvers
Anders Helgeland, *Research Manager*
Janet Martha Blatny, *Research Director*

The document is electronically approved and therefore has no handwritten signature.

Summary

Modeling of explosions and implosions under water is important for design of vehicles and installations both under water and on the sea surface. There exists simple models, often in the form of empirical calibrations, for the loads experienced at a given distance from an explosion. These models, however, are often insufficient, for example if one is interested in the response of a ship to an explosion at short or moderate distances from the ship. It is therefore necessary to be able to simulate such problems with high accuracy, and account for the interactions between explosion gases, water, air and the ship simultaneously. This is a very difficult problem, but modern methods and computational resources are able to perform such simulations, which provide valuable insights into realistic underwater explosion scenarios.

This report is concerned with the implementation of a method for simulation of explosions and implosions under water in the flow solver "Charles", which is used at the Norwegian Defence Research Establishment (FFI). The extended simulation capabilities this implementation provides will strengthen the ability to simulate these problems at FFI, and increase FFI's knowledge about underwater explosion problems.

The "finite volume method with exact two-phase Riemann solver" (FIVER) has been implemented in Charles. This method is especially suited to simulate interactions between materials with very different properties, under the extreme thermodynamic conditions following immediately after detonation of a high explosive. The method is of a type that is readily implemented in the flow solver. In this work, the method has been implemented and tested for one-dimensional problems. In future work, the flow solver will be developed further, and the method will be implemented for two and three dimensions, so that realistic problems can be simulated.

Sammendrag

Modellering av eksplosjoner og implosjoner under vann er viktig for design av farkoster og installasjoner både under vann og på havoverflaten. Det finnes enkle modeller, ofte i form av empiriske kalibreringer, for beregning av lastene opplevd ved en gitt avstand fra en eksplosjon. Disse er ofte ikke tilstrekkelige, for eksempel dersom man ønsker å vite responsen til et skip på lastene fra en eksplosjon i nærheten av skipet. Det er derfor nødvendig å kunne simulere slike problemstillinger med høy nøyaktighetsgrad, og ta hensyn til interaksjonen mellom eksplosjonsgasser, vann, luft og skipet samtidig. Dette er et svært vanskelig problem, men moderne metoder og regneressurser er i dag i stand til å simulere disse problemene, og gir viktig innsikt i realistiske scenarioer.

Denne rapporten dreier seg om implementering av en metode for simulering av eksplosjoner og implosjoner under vann i strømningsløseren "Charles", som er i hyppig bruk ved Forsvarets forskningsinstitutt (FFI) i dag. Denne utvidede simuleringsevnen vil gjøre FFI i bedre stand til å simulere slike problemer og bygge opp kompetansen på dette området.

Metoden "finite volume method with exact two-phase Riemann solver (FIVER)" har blitt implementert i Charles. Denne metoden er spesielt egnet til å simulere interaksjon mellom materialer som har svært ulike egenskaper, under de ekstreme tilstandene som oppnås umiddelbart etter detonasjon av et høyeksplosiv. Metoden er av en type som lett lar seg implementere i strømningsløseren. I dette arbeidet har metoden blitt implementert og testet for endimensjonale problemer. I videre arbeid vil strømningsløseren videreutvikles, og metoden vil bli implementert for to og tre dimensjoner, slik at realistiske problemstillinger kan simuleres.

Contents

1 Introduction

One of the goals in FFI project 1447 "Simulering og modellering av strømninger og materialer" is to implement a model that can simulate underwater explosion events near ships, and predict their response to the resulting loads. The ability to simulate such events is of importance to the military, and also for offshore and subsea industries. Additionally, removal of WWII naval mines is still necessary in Norwegian coastal waters, and improved simulation capabilities of underwater explosions are important for this purpose as well.

This document is intended to form a basis for the numerical modeling and simulations of underwater explosions in FFI project 1447. Key phenomena in an underwater explosion event will be discussed, and empirical models for limited parts of the problem will be introduced. The empirical models have useful applications, but cannot be used to obtain new information about underwater explosions. Computational fluid dynamics (CFD) models, on the other hand, can provide new information, but they must accurately model a challenging, multi-physics, problem. Common CFD software in use today are not able capture the physical processes involved in an underwater explosion in a satisfactory manner. Therefore, it is necessary to develop and implement new models that are applicable to simulations of underwater explosion events. In this report, several candidate models will be reviewed. The model that is found most suitable will be integrated in an already existing framework for solving fluid mechanical problems by means of computational fluid mechanics, at the Norwegian Defence Research Establishment (FFI). The selected model will be implemented as an extension to the flow solver "Charles".

This report is structured as follows. First, in chapter 2, a brief discussion and an introduction of the physical phenomena involved in underwater explosions are given. Next, in chapter 3, different modeling approaches are discussed, with emphasis on sharp interface Eulerian finite volume methods, since this is the type of model that has been chosen to implement in the Charles code. Under the modeling section, in section 3.1, the various equations of state that have been used to describe the materials involved in underwater explosions are listed. A few theoretical and empirical simplified models for different parts of the problem are provided in chapter 4. Then, the model for simulation of underwater explosions is described in detail in chapter 5. A range of numerical, one-dimensional, tests are performed, and the numerical results are compared with exact Riemann problem solutions in chapter 6. Finally, concluding remarks are given in chapter 7.

2 Underwater explosions

Despite extensive studies, detonation of explosives submerged in water is a process that is still not completely understood. The problem features various complicated physical processes, including chemical reactions during detonation, multi-phase and multi-material flows, cavitation, fluid-structure interaction and more. One of the most influential works on the subject is the book by Cole (1948), which contains a discussion of many of the processes occurring during underwater explosions (UNDEX). Cole's work was previously summarized in the report of Kiran (2016). Kiran's report provides a brief overview of some of the topics relevant to underwater explosions, and introduces several theoretical and empirical models for parameters of interest. The discussion in this report is limited to a selection of phenomena during underwater explosions that are particularly important for high-fidelity computational fluid dynamics UNDEX modeling.

In the case where a high-explosive charge is detonated under water, the process starts with a detonation wave that propagates through the explosive material, converting the explosive material primarily to gases and thereby releasing high amounts of energy in a small volume. When the detonation wave reaches the edge of the explosive, the detonation product gases will begin to expand since the gas pressure is higher than that in the surrounding water. Therefore, a shock wave will be driven outwards in the water, while a rarefaction wave will be reflected back into the dense detonation product gases. The rate of expansion and shock wave strength are often used in aquarium tests for explosive material testing (Lozano et al., 2020).

During the gas expansion, the gas pressure is gradually reduced and eventually falls below the pressure of the surrounding water. At this point, the gas acceleration is reversed, the radial velocity decreases to negative values and the gas bubble will begin to contract. As the bubble becomes smaller, the pressure increases again, and the process repeats, leading to the phenomenon of bubble oscillation. These oscillations are accompanied by strong pressure waves in the surrounding water, and can be very important for the loads imposed on e.g. ships or pipes near the explosion. Approximate expressions for the bubble oscillation period can be found in (Kiran, 2016). Bubble oscillation generally occurs on a much longer time-scale (seconds) than shock-formation and propagation (milliseconds) (Costanzo, 2011). Along with the oscillation, the bubble will in most cases migrate upwards due to buoyancy. The upward migration occurs primarily while the bubble is in a contraction phase (Rosseland, 1950). The oscillation thus continues either until the bubble has lost all its energy, reached the surface, or is completely broken up.

The detonation product gases are generally non-condensable, and this makes UNDEX bubble dynamics different from bubbles generated by cavitation, lasers, or sparks. The minimum bubble size is therefore larger, and the bubble oscillation has a shorter period.

In many configurations, the effect of buoyancy can be important for the bubble dynamics. Due to the higher pressure at the bottom of the bubble, the bubble collapse is asymmetrical and the bottom side develops into a water jet penetrating into the bubble (Holt, 1977). This can occur multiple times during the bubble oscillation, as sketched in figure 2.1. Water jet formation also occurs with bubbles located close to solid boundaries, in which case the jet is directed towards the boundary. Additionally, the bubble will migrate towards the boundary due to the Bjerknes effect (Blake et al., 1986; Johnsen and Colonius, 2009). The water jet affects the pressure waves emanating from the bubble, and can therefore be important for structural loads. In the worst case, the water jet can impact directly on the solid surface. More commonly, the water jet will impact on the water on the other side of the bubble. The water hammer pressure can be approximated as

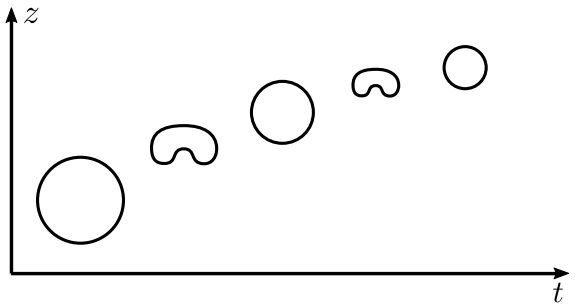

Figure 2.1 Sketch of bubble shape, size and position over time. During bubble collapse, a water jet forms on the bottom side of the bubble.

(Huang et al., 1973; Johnsen and Colonius, 2009):

$$p_{\text{wh}} \approx \rho_L c_L v_j \frac{\rho_s c_s}{\rho_s c_s + \rho_L c_L}, \tag{2.1}$$

where ρ_L is the liquid density, c_L is the speed of sound in the liquid, v_j is the jet velocity, ρ_s is the solid density, and c_s is the solid speed of sound. Thus, if the jet impacts on water, with $\rho_L \approx 1000$ kg/m^3, $c_L \approx 1500$, the water hammer pressure is $1.5 \times 10^6 v_j$, which is $O\left(10^8\right)$ Pa even for a relatively low jet velocity of 67 m/s. This rough estimate demonstrates that the water hammer pressure can be significant for loads near the impact point. Predicting the bubble dynamics and the resulting pressure waves are generally among the most challenging parts of simulating UNDEX events.

If the explosion occurs sufficiently close to the surface, a shock wave will be driven into the air above the water, and a rarefaction wave will be reflected downwards. This can lead to the phenomenon referred to as bulk cavitation, where a large amount of water near the surface cavitates to form a mix of water vapour and droplets (Costanzo, 2011). When this cavitated region collapses, a pressure wave is released in a process that is very similar to the bubble collapse discussed above. Equation (2.1) again gives the order of magnitude of the pressure pulse, which can be large.

3 Modeling approaches for underwater explosions

Simulating underwater explosions is challenging due to the necessity to accurately predict the movement of the bubble-water interface over a period of time that is long compared to the time-scales of the shock and rarefaction waves present in the problem. Multi-material flow models are typically prone to pressure oscillations around the material interface (Abgrall and Karni, 2001), which can be particularly problematic for problems where this interface is important, such as in underwater explosions. Many models for simulating underwater explosions have been proposed, with varying degrees of robustness, computational efficiency, and ease of implementation. A brief description of a few of these models is given below.

The methods can be divided into models that simulate the internal gas-dynamics of the gas bubble along with the wave-propagation in water, and those that do not resolve the waves, but rather compute the size of the gas bubble and infer velocity and pressure based on a potential flow assumption. The first kind can be further divided into front-tracking methods and interface-capturing methods. In front-tracking methods, the position of the (sharp) gas-water interface is described either with a purely Lagrangian approach or with an additional field variable (e.g. level-set and volume of fluid methods). In the interface capturing methods, where the materials are allowed to mix and the interface becomes smeared over a number of computational cells, the mixture composition is tracked with an additional field variable that typically represents the volume fraction, mass fraction, or an equation of state parameter.

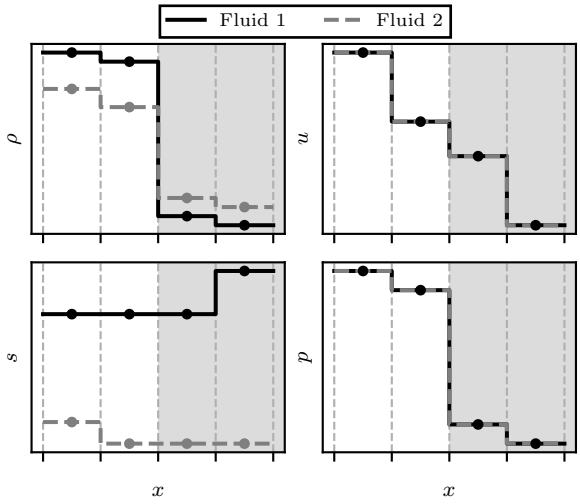

Figure 3.1 Example of the density, velocity, entropy and pressure in the ghost-fluid method. The shaded region is where fluid 2 is the "real" fluid. The pressure and entropy are defined by the equation of state for each fluid from mass density ρ and internal energy e. In the ghost fluid region, entropy is defined by one-sided extrapolation, while ρ is given by the equation of state relation $\rho = \rho(s, p)$. Fluxes are computed separately for the two fluids based on ρ, u, p.

In the Eulerian, sharp interface, category, the ghost fluid method (Fedkiw et al., 1999), and various extensions of it have been very popular for two-phase or two-component flow. Some examples of their use for gas-water interaction are Liu et al. (2003); Xie et al. (2007); Terashima and Tryggvason (2009); Park (2019). The ghost-fluid method in its simplest form defines two fluids for

the whole domain, and a level-set function defines which fluid that is the "real" fluid in each point. Correspondingly there also exists a "ghost-fluid" in each point. This is illustrated in figure 3.1. A time-step in the ghost-fluid method proceeds as following. First, the pressure is defined by the equation of state in every point. The pressure and velocity of the ghost fluid are set to the pressure and velocity of the real fluid in every point. Then entropy of each fluid is extrapolated into the ghost-fluid region. The method then computes a ghost-fluid density based on the equation of state relation $\rho = \rho(s, p)$, where s is the entropy. In order to suppress "overheating", the entropy at the real-fluid side of the interface is overwritten by the entropy one step further away from the interface, thus defining a new real-fluid density beside the interface. Finally, the method applies standard methods to compute fluxes separately for the two fluids based on ρ, u, and p, which have now been defined everywhere for both fluids. After the fluid variables have been stepped forward in time, the level-set function is stepped forward to define a new position for the interface. Other choices are also possible for defining the ghost-fluid variables, and yields different properties for the method, especially the amount of overheating (Fedkiw et al., 1999).

Liu et al. (2003) demonstrated that the original ghost-fluid method does not robustly capture the interaction between a shock wave and a material discontinuity. While acceptable solutions could be obtained for somewhat similar materials, problems involving gas-water interfaces needed many time-steps before reaching correct interface conditions, leading to errors in the interface locations, transmitted shock wave strengths and rarefaction fan widths. Liu et al. (2003) proposed to define the ghost-fluid states based on a two-shock approximation to the Riemann problem at the interface. In their method, the ghost-fluid state and the real fluid density next to the interface are set by the solution to this two-shock approximation. Liu et al. (2003) demonstrated that this alternative ghost-fluid method yields improvements for problems involving shock wave - material interface interactions. A simplification of this method was proposed in Xie et al. (2007), where ρc is assumed constant on each side of the interface, yielding an explicit method. The authors claim that the method is appropriate for problems without strong rarefactions.

Farhat et al. (2008) introduced the finite volume method with exact two-phase Riemann solver (FIVER) for simulating underwater implosions. The model was initially referred to as a ghost-fluid method. They later recommended not to view the method as a ghost-fluid method since ghost points are not explicitly used (Farhat et al., 2012). The model was motivated by the observation that the ghost-fluid method failed in many water-gas problems, and that it was not applicable to general equations of state. In some aspects, the idea behind the method of Farhat et al. (2008) resembles that of Liu et al. (2003). It relies on solving an exact Riemann problem at the material discontinuities, as illustrated in figure 3.2. Having found the exact solution to the two-phase Riemann problem, the method proceeds by using this solution to define two new, single-fluid, Riemann problems, which are used to compute the fluxes into the left and right control volumes. The flux is computed differently for the left and right sides, and thus the method is only approximately conservative. Once the fluid variables have been updated, the level-set function is stepped forward in time. At the end of each time-step, control volumes that have undergone a material change are updated with the solution of the exact Riemann problem, in order to preserve a sharp resolution of the contact discontinuity. The method was further developed and tested in Farhat et al. (2012), Main and Farhat (2014), and Main et al. (2017). In Farhat et al. (2008) the method is used to simulate an underwater implosion, and the numerical results compare well to experimental results during the bubble rebound. The method was also recently used to study shock wave lithotripsy (Wang, 2017).

Diffuse interface (interface capturing) approaches have also been used for gas-water interactions. For example, three such models were considered by Schmidmayer et al. (2020) for simulating

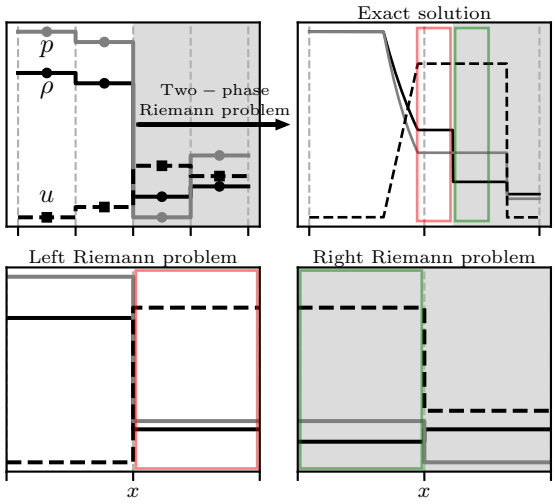

Figure 3.2 Illustration of the central component of the FIVER algorithm. The method computes the exact solution to the two-phase Riemann problem, and uses the exact solution around the contact discontinuity to construct two new Riemann problems that are then used to compute the fluxes for the left and right control volumes. The regions with a gray background correspond to a different material than the regions with a white background.

bubble collapses. The three methods were the five-equation model of Allaire et al. (2002), the thermodynamically consistent model of Kapila et al. (2001) and the six-equation model of Saurel et al. (2009). The advantages of diffuse interface models are that they can utilize the same flux-schemes for the whole domain, they have the ability to simulate the appearance of interfaces, and can perform simulations of multiphase mixtures with dynamically changing material compositions (Saurel et al., 2009). Diffuse interface models require closure relations in regions where the fluids are mixed. The details of the closures are important for the performance of these schemes. For example, Abgrall and Karni (2001) demonstrated that for a mix of ideal gases, a mixture equation of state defined by averaging $(\gamma - 1)^{-1}$ to define an effective gamma is the one choice that does not introduce pressure oscillations over a material discontinuity. Additionally, the numerical discretization must satisfy certain properties to avoid these oscillations. Allaire's model (Allaire et al., 2002) consists of a separate mass conservation equation for each species, along with shared momentum and total energy equations, and an advection equation for the volume fraction of one of the species. With isobaric closure for the mixture equation of state, the model was shown to work well for many different one-dimensional problems. However, Schmidmayer et al. (2020) showed that the bubble size in a bubble collapse problem was not well captured with Allaire's model. Kapila's model (Kapila et al., 2001) includes an additional term,

$$\frac{\rho_2 c_2^2 - \rho_1 c_1^2}{\rho_2 c_2^2 \alpha_2^{-1} + \rho_1 c_1^2 \alpha_1^{-1}}, \tag{3.1}$$

in the volume fraction equation, where ρ_1 is the intrinsic density of species 1, ρ_2 is the intrinsic density of species 2, $c_{1,2}$ are the individual sound speeds and $\alpha_{1,2}$ are the volume fractions. Schmidmayer et al. (2020) showed that this additional term increases the interface velocity, keeping the interface sharper, and thus improving the quality of the bubble collapse simulation. Kapila's

model unfortunately suffers from beeing unstable in presence of strong shocks or rarefactions around the interface. Schmidmayer et al. (2020) therefore considered the six-equation model of Saurel et al. (2009) to be the most suitable model of the three alternatives, as the simulation results for this model were as good as with Kapila's model, but without the unstable behaviours.

The six-equation model of Saurel et al. (2009) solves the equation set

$$\partial_t \begin{bmatrix} \alpha_1 \\ \alpha_1\rho_1 \\ \alpha_2\rho_2 \\ \rho u \\ \alpha_1\rho_1 e_1 \\ \alpha_2\rho_2 e_2 \end{bmatrix} + \partial_x \begin{bmatrix} \alpha_1 u \\ \alpha_1\rho_1 u \\ \alpha_2\rho_2 u \\ \rho u u + p \\ \alpha_1\rho_1 e_1 u \\ \alpha_2\rho_2 e_2 u \end{bmatrix} + \begin{bmatrix} -\alpha_1 \\ 0 \\ 0 \\ 0 \\ \alpha_1 p_1 \\ \alpha_2 p_1 \end{bmatrix} \partial_x u = \begin{bmatrix} \mu(p_1 - p_2) \\ 0 \\ 0 \\ 0 \\ -\mu p_I (p_1 - p_2) \\ \mu p_I (p_1 - p_2) \end{bmatrix}, \tag{3.2}$$

where p_I is the interface pressure, and μ is the pressure relaxation coefficient. Under stiff pressure relaxation, this model tends to Kapila's model (Saurel et al., 2009). In Saurel et al. (2009), it is shown that this method yields excellent results for various shock-tube problems, including cavitation problems, as well as for the commonly used air-shock helium-bubble interaction test.

A sharp-interface model is preferable for the current application, because this allows the simulation to keep the interface between air and water sharp over several bubble pulsation periods. Thus the most attractive candidate is the FIVER method Farhat et al. (2008, 2012), due to its applicability to all parts of the underwater explosion phenomenon.

An alternative to the approaches discussed above is to use Lagrangian descriptions for parts of the fluid domain or the entire fluid domain. An example of this is the work of Ball et al. (2000), who studied the shock-induced collapse of an air-bubble in water using a Voronoi tesselation of the fluid domain, defined by the positions of fluid particles. In this approach, the particles are initially assigned a material and mass, and these remain unchanged over the simulation. The particles are advected at the local fluid velocity, and Ball et al. (2000) opted to redefine the Voronoi tesselation at every fifth time step. The model was used in Turangan et al. (2008) to simulate the collapse of a water bubble near an aluminium wall, and shock-induced collapse of air bubbles in the context of shock wave lithotripsy.

Lagrangian descriptions have the advantage of keeping material interfaces sharp, since the methods do not allow material mixing. However, the methods often struggle with mesh distortion by strong velocity shears, and often excessively small time-steps (Pishevar and Amirifar, 2010). A solution to these problems is periodic remeshing, i.e. as done at every fifth time step in Ball et al. (2000).

Pishevar and Amirifar (2010) used an arbitrary Lagrangian-Eulerian (ALE) method. The Eulerian grid around the material interface was transformed by the local flow velocity, thus keeping the grid aligned with the gas-water interface. An interface smoothing procedure was applied to dampen grid-induced surface irregularities, and they also applied remeshing to limit the effect of mesh distortion. In this way, the ALE method could be used similarly to the purely Lagrangian approaches, while utilizing the strengths of the Eulerian methods for the parts of the domain away from the material interface.

Another approach for modeling bubble dynamics is to use potential-theory based models. Some examples can be found in Blake et al. (1986); Klaseboer et al. (2005); Liu et al. (2018). In these approaches, wave propagation is typically not included in the model and they can therefore not be used to simulate the shock waves occurring in UNDEX events. However, the pressure pulses due to bubble collapse can be modeled in this framework (Blake et al., 1986). The fluid is assumed

incompressible, inviscid and irrotational, and thus the velocity field is given by

$$\mathbf{u} = \nabla\phi, \tag{3.3}$$

where ϕ is a velocity potential that satisfies

$$\nabla^2\phi = 0. \tag{3.4}$$

Green's second identity gives (Klaseboer et al., 2005)

$$c(\mathbf{x})\phi(\mathbf{x}) + \int_s \left[\phi(\mathbf{y})\frac{\partial G(\mathbf{x},\mathbf{y})}{\partial \mathbf{n}(\mathbf{y})} - \frac{\partial \phi(\mathbf{y})}{\partial \mathbf{n}(\mathbf{y})}G(\mathbf{x},\mathbf{y})\right] ds(\mathbf{y}), \tag{3.5}$$

where s denotes the boundary, G is the free space Green's function and c is the solid angle of the fluid domain at point $\mathbf{y}$. In this approach, computational meshes are only required on the surfaces of the gas bubble and other boundaries present in the problem. These methods are therefore significantly less computationally demanding than the methods discussed above. Once the potential ϕ has been determined, the position of the boundary points are updated based on the local velocity. Thus the solution is marched forward in time, and properties of interest, such as the pressure at a given point, can be computed from the potential. In Blake et al. (1986), this approach was used to study the collapse of bubbles near rigid boundaries. Klaseboer et al. (2005) simulated the collapse of bubbles near resilient or rigid structures, while Liu et al. (2018) simulated the response of a ship to the combined loading due to an UNDEX event and surface waves.

The above discussion has introduced some of the methods that have been used to study UNDEX events, but is by no means an exhaustive list. In the rest of this report, the FIVER method (Farhat et al., 2008, 2012) will be used, as it is straightforward to build into the Charles code, and has been shown to work well for the problem of interest here.

3.1 Equations of state

In the following, some of the most commonly used equations of state for the materials involved in UNDEX events are introduced. These define the relationship between pressure, density and internal energy for water, air and detonation product gases.

3.1.1 Equations of state for water

In the context of UNDEX modeling, the two most widely used equations of state (EOS) are Tait's EOS and the stiffened gas EOS. The former is usually given as

$$p = K_0\left[\left(\frac{\rho}{\rho_0}\right)^{\theta} - 1\right] + p_0, \tag{3.6}$$

where K_0 and θ are, in general, functions of temperature and pressure, ρ_0 is the reference density and p_0 is the reference pressure. In Chandran and Salih (2019), the constant values $K_0 = 3 \times 10^8$ and $\theta = 7$ were used. An alternative form was used in Liu et al. (2003); Xie et al. (2007), where

$$\rho e = \frac{p}{\gamma - 1} + \frac{\gamma\,(B - A)}{\gamma - 1}, \tag{3.7}$$

where the EOS constants are $A = 10^5$ Pa, $B = 3.31 \times 10^8$ Pa, and the adiabatic index $\gamma = 7.15$. The stiffened gas equation of state is given by

$$p = (\gamma - 1)\,\rho e - \gamma\pi \tag{3.8}$$

where π is a pressure offset. The alternative form of Tait's EOS (equation (3.7)) is immediately seen to be equal to a stiffened gas. The stiffened gas EOS was used in e.g. Farhat et al. (2008, 2012) with $\gamma = 4.4$ and $\pi = 6 \times 10^8$ Pa. In Johnsen and Colonius (2009), the values $\gamma = 6.68$ and $\pi = 4050$ atm. were used.

Wang et al. (2014) used an split polynomial equation of state for water. Pressure is given in terms of density and internal energy as

$$p = \begin{cases} A_1\mu + A_2\mu^2 + A_3\mu^3 + (B_0 + B_1\mu)\rho_0 e & \text{if } \rho > \rho_0 \\ T_1\mu + T_2\mu^2 + B_0\rho_0 e & \text{if } \rho \leq \rho_0 \end{cases}, \tag{3.9}$$

where $\mu = \rho/\rho_0 - 1$, and $A_1 = 2.2 \times 10^9$ Pa, $A_2 = 9.54 \times 10^9$ Pa, $A_3 = 1.457 \times 10^9$ Pa, $B_0 = 0.28$, $B_1 = 0.28$, $T_1 = 2.2 \times 10^9$ Pa, $T_2 = 0$ Pa, and $\rho_0 = 999$ kg/m^3.

In some approaches, cavitation have been modeled by segmenting the equation of state, either by pressure or density. In Pishevar and Amirifar (2010), the authors used Tammann's EOS for water:

$$p = (p_0 + B)\left(\frac{\rho}{\rho_0}\right)^{\gamma} - B, \tag{3.10}$$

with $p_0 = 10^5$ Pa, $\rho_0 = 1000$ kg/m^3 and $\gamma = 7.15$. Tammann's EOS is on the same form as Tait's EOS. To include cavitation, equation (3.10) was applied for pressures above 3169 Pa, and

$$p = \max\left(p_\varepsilon,\ p_{\text{sat}} + p_{gl}\ln A\right) \tag{3.11}$$

was applied otherwise. Here p_ε is a very small lower pressure limit, while $p_{\text{sat}} = 3169$ Pa,

$$p_{gl} = \frac{\rho_g c_g^2 \rho_l c_l^2 (\rho_g - \rho_l)}{\rho_g^2 c_g^2 - \rho_l c_l^2}, \tag{3.12}$$

and

$$A = \frac{\rho_g c_g^2 \rho_l c_l^2 (\rho_l + \alpha(\rho_g - \rho_l))}{\rho_l\left(\rho_g^2 c_g^2 - \alpha(\rho_g c_g^2 - \rho_l c_l^2)\right)}, \tag{3.13}$$

where ρ_l and ρ_g are the densities of liquid water and water vapor, respectively, which were assumed constant. Since these were assumed constant, the volume fraction α could be computed from the the mixture density ρ.

3.1.2 Equations of state for air

Under most conditions, air can be modeled with the ideal gas equation of state. It is

$$p = (\gamma - 1)\rho e, \tag{3.14}$$

where the adiabatic index, γ, is usually set to 1.4.

3.1.3 Equations of state for detonation products

The most commonly used equation of state for detonation products is the Jones-Wilkins-Lee equation of state. It is given by

$$p = A\left(1 - \frac{\omega\rho}{R_1\rho_0}\right)e^{-R_1\rho_0/\rho} + B\left(1 - \frac{\omega\rho}{R_2\rho_0}\right)e^{-R_2\rho_0/\rho} + \omega\rho(e - e_0). \tag{3.15}$$

Farhat et al. (2012) used the following parameters for TNT: $A = 3.712 \times 10^{11}$ Pa, $B = 3.230 \times 10^9$ Pa, $R_1 = 4.15$, $R_2 = 0.95$, $\omega = 0.3$, $\rho_0 = 1630$ kg/m^3, and $e_0 = 0$.

4 Simplified theoretical and empirical models

This section contains empirical and theoretical models for some aspects of UNDEX events. In particular, models for the blast wave profile and models for the gas bubble pulsation are listed. These are useful for model evaluation, or can serve as initial conditions or input for fluid-structure test problems. While they are not used for these purposes in this report, they will be used in future studies at FFI.

4.1 Blast wave parametrization

For charges located sufficiently far from a measuring point, the pressure-time profile is often approximated with the aid of empirical calibrations. These approximations originate from a set of experiments conducted by the Naval Ordnance Laboratory in the 1950s and 1960s (Costanzo, 2011). For example, the following blast wave approximation was used in Wang et al. (2014) to evaluate the results of their numerical simulations:

$$p(t) = p_{\mathrm{m}} \exp\left(-t/\theta\right), \tag{4.1}$$

where p_{m} is the peak pressure and θ is a decay time scale. The peak pressure is given as

$$p_{\mathrm{m}} = k_1 \left(\frac{W^{1/3}}{R}\right)^{\alpha_1}, \tag{4.2}$$

where k_1 and α_1 are constants related to the explosive charge type, R is the radial distance from the charge center, and W is the charge mass. The decay time scale is given by

$$\theta = k_2 W^{1/3} \exp\left(\frac{W^{1/3}}{R}\right)^{\alpha_2}, \tag{4.3}$$

where k_2 and α_2 are constants related to the explosive charge type. For TNT, Wang et al. (2014) used $k_1 = 52.16 \times 10^6$ Pa, $\alpha_1 = 1.13$, $k_2 = 96.5 \times 10^{-6}$, and $\alpha_2 = -0.22$.

4.2 Bubble dynamics

4.2.1 Rayleigh-Plesset model

A simple model for the bubble pulsation developed by Rayleigh is (Li et al., 2018)

$$\ddot{R}R + \frac{3}{2}\dot{R}^2 = \frac{p_0}{\rho_L}\left(\frac{R_0}{R}\right)^{3\gamma} - \frac{p_\infty}{\rho_L}, \tag{4.4}$$

where R denotes the bubble radius, dots are used to denote differentiation with respect to time, p_∞ is the far-field pressure and ρ_L is the liquid density. An estimate of the initial radius R_0 for TNT was given in Li et al. (2018), and ensures that the model correctly predicts the maximum bubble radius observed in experiments.

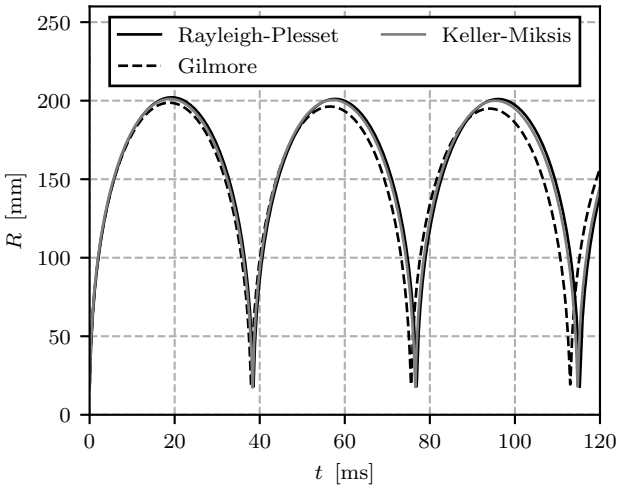

Figure 4.1 Evolution of the bubble radius R with three different models for the test case considered in Li et al. (2018), where $p = 49 \times 10^6$ Pa at the bubble surface, and the initial bubble radius is 17.2 mm. The water density is set to 998 kg/m^3, the far-field pressure $p_\infty = 1$ atm, and the equation of state parameters used are $\gamma = 1.25$, $n_T = 7.15$ and $B = 3046 \times 10^5$ Pa.

4.2.2 Gilmore model

A slightly more sophisticated model, the Gilmore model (Gilmore, 1952), was also used in Li et al. (2018). Here, compressibility effects are included, and the equation for the bubble radius is

$$\left(1 - \frac{\dot{R}}{C}\right) R\ddot{R} + \frac{1}{2}\left(3 - \frac{\dot{R}}{C}\right)\dot{R}^2 = \left(1 + \frac{\dot{R}}{C}\right) h + \left(1 - \frac{\dot{R}}{C}\right)\frac{R}{C}\frac{dh}{dt}, \tag{4.5}$$

where h is the isentropic enthalpy difference between ambient water and water at the bubble surface pressure. It is given by

$$h = \int_{p(r=\infty)}^{p(r=R)} \frac{dp(\rho)}{\rho} = \frac{(p_\infty + B)(n_T - 1)}{\rho_\infty n_T}\left[\left(\frac{p + B}{p_\infty + B}\right)^{(n_T-1)/n_T} - 1\right], \tag{4.6}$$

$$\frac{dh}{dt} = \frac{1}{\rho_\infty (p_\infty + B)}\left(\frac{p + B}{p_\infty + B}\right)^{-1/n_T} p_0 \left(\frac{R_0}{R}\right)^{3\gamma} \dot{R} \tag{4.7}$$

and

$$C = c_0 \left(\frac{p + B}{p_\infty + B}\right)^{(n_T-1)/(2n_T)}, \quad c_0^2 = \frac{p_\infty + B}{\rho_\infty} n_T, \tag{4.8}$$

where C is the speed of sound at the bubble boundary, and c_0 is the speed of sound in the ambient water.

4.2.3 Keller-Miksis model

Keller and Miksis (1980) derived a model for forced oscillations of a bubble in an incident sound field, and Schmidmayer et al. (2020) used this model for testing numerical models for simulating

bubble implosions. It includes the effects of surface tension, viscosity and acoustic radiation. In absence of forcing, the model for the bubble radius evolution is

$$\ddot{R}\left(\frac{4\mu}{\rho} - R(\dot{R} - c)\right) = \frac{1}{2}\dot{R}^3 + \dot{R}\Delta(R) - c\left(\frac{3}{2}\dot{R}^2 + \frac{4\mu\dot{R}}{\rho R} + \frac{2\sigma}{\rho R} - \Delta(R)\right) + R\dot{R}\Delta'(R), \tag{4.9}$$

where σ is the surface tension, μ is the dynamic viscosity of the fluid, c is the speed of sound, $'$ denotes differentiation, and

$$\Delta(R) = \rho^{-1}\left[kR^{-3\gamma} + p_v - p_\infty\right], \tag{4.10}$$

where k is an equation of state constant that relates the bubble pressure, p_b, constant vapor pressure, p_v, and density as

$$p_b = p_v + kR^{-3\gamma}. \tag{4.11}$$

Figure 4.1 shows a comparison of the Rayleigh-Plesset model, the Keller-Miksis model and the Gilmore model.

5 Model for simulating underwater explosions

In this report, following the approach of Farhat et al. (2008, 2012), FIVER is used to simulate underwater explosions. FIVER is a model for the dynamics of two immiscible fluids, where the exact solution of the two-fluid Riemann problem is utilized when computing the flux across faces with material changes. The model has two central components; (1) the exact multi-material Riemann solver, which has to be efficient and robust; (2) the two-fluid finite volume model, with an approximate single component Riemann solver or any other flux scheme.

The basis of both components are the Navier-Stokes equations, which can be written

$$\partial_t \rho + \partial_k (\rho u_k) = 0, \tag{5.1}$$

$$\partial_t (\rho u) + \partial_k (\rho u_i u_k + p\delta_{ik}) = \partial_j \mu \left(\partial_i u_j + \partial_j u_i - 2\delta_{ij}\partial_k u_k/3\right) \tag{5.2}$$

$$\partial_t (\rho E) + \partial_k ((\rho E + p)u_k) = \partial_j \left(u_i \mu \left(\partial_i u_j + \partial_j u_i - 2\delta_{ij}\partial_k u_k/3\right)\right) - \partial_k (\lambda \partial_k T) \tag{5.3}$$

where μ is the dynamic viscosity, δ_{ij} is the Kronecker delta, $E = e + u_i u_i/2$ is the specific total energy, where e is the specific internal energy, λ is the heat conductivity and T is the temperature. In the rest of this report, the viscous terms in equations (5.2) and (5.3), i.e. the right-hand sides, will ignored, as they are not important for the problems under consideration here.

Along with equations (5.1) to (5.3), the two-fluid model requires an equation to keep track of the where the interface is located, as well as an equation of state for both fluids. Here, the level-set equation

$$\partial_t (\rho z) + \partial_k (\rho z u) = 0, \tag{5.4}$$

is used to describe the material interface, where z is a signed distance function, which for each computational point describes the minimum distance to the interface. The signed distance function has the property that if $z(\mathbf{x}_1)z(\mathbf{x}_2) < 0$, $\mathbf{x}_1$ and $\mathbf{x}_2$ are two position vectors, then there is a material interface between $\mathbf{x}_1$ and $\mathbf{x}_2$.

5.1 Exact Riemann solver

The two-fluid Riemann problem can be written

$$\partial_t \mathbf{q} + \partial_x \mathbf{f}(\mathbf{q}) = 0, \tag{5.5}$$

with initial conditions

$$\mathbf{q}(\mathbf{x}, 0) = \begin{cases} \mathbf{q}_L & \text{if } x \leq 0 \\ \mathbf{q}_R & \text{if } x > 0 \end{cases}, \tag{5.6}$$

where $\mathbf{q} = (\rho, \rho u, \rho E)^T$ is the state vector and $\mathbf{f}(\mathbf{q}) = (\rho u, \rho u^2 + p, \rho E u + p u)^T$ is the flux of $\mathbf{q}$.

The left and right states are allowed to have different equations of state, but it is assumed that both can be written in Mie-Gruneisen form. The approach here follows that of Hennessey et al. (2020), and the following form of a Mie-Gruneisen EOS is used:

$$e = A(\rho)p + B(\rho). \tag{5.7}$$

With this notation, the speed of sound is

$$c^2 = \frac{\left[1 - \rho^2 A'(\rho)\right] - \rho^2 B(\rho)}{\rho^2 A(\rho)}, \tag{5.8}$$

where $'$ denotes differentiation with respect to ρ.

The exact solution of the Riemann problem consists of a set of waves emanating from the discontinuity at $x = 0$. These can be either rarefaction waves, shock waves or contact waves. The approach for finding the exact solution of the Riemann problem is to identify the type of waves present in the solution, and then determine the strength of the waves by requiring that both pressure and velocity match on both sides of the contact discontinuity. In general, this requires an iterative method, and in addition, the jump over the rarefaction wave must be computed using a numerical quadrature.

5.1.1 Pressure and velocity jumps as functions of density

For rarefaction waves, the jumps in pressure and velocity vary with density as (Hennessey et al., 2020):

$$\frac{dp}{d\rho} = c^2, \quad \frac{du}{d\rho} = \mp\frac{c}{\rho}. \tag{5.9}$$

The pressure equation can be solved by substituting equation (5.8) and integrating. As in Hennessey et al. (2020), this gives an equation

$$p(\rho, \rho_0, p_0) = G^{\mathrm{R}}(\rho, \rho_0, p_0) = \frac{\mu(\rho_0)p_0}{\mu(\rho)} + \frac{H(\rho) - H(\rho_0)}{\mu(\rho)}, \tag{5.10}$$

where

$$\mu(\rho, \rho_0) = A(\rho)\exp\int_{\rho}^{\rho_0} \frac{1}{\hat{\rho}^2 A(\hat{\rho})} d\hat{\rho}, \tag{5.11}$$

and

$$H(\rho, \rho_0) = \int_{\rho}^{\rho_0} \frac{\mu(\hat{\rho}, \rho_0)B'(\hat{\rho})}{A(\hat{\rho})} d\hat{\rho}, \tag{5.12}$$

where the last equation differs from the expression in Hennessey et al. (2020) by a factor $\hat{\rho}^2$ in the integrand. This is likely a typo in Hennessey et al. (2020). In the above equations, ρ_0 is some chosen reference density. For the velocity jump, the integration is not as easily carried out, but can be solved numerically. The expression is

$$F^{\mathrm{R}}(\rho, \rho_0) = -\int_{\rho}^{\rho_0} \left[\frac{(1 - \hat{\rho}^2 A'(\hat{\rho})) - \hat{\rho}^2 B'(\hat{\rho})}{\hat{\rho}^2 A(\hat{\rho})}\right]^{1/2} \frac{d\rho}{\rho}. \tag{5.13}$$

Thus, for a known change in density, the pressure and velocity are

$$p(\rho, \rho_0, p_0) = G^{\mathrm{R}}(\rho, \rho_0, p_0), \quad u(\rho, \rho_0) = u_0 \mp F^{\mathrm{R}}(\rho, \rho_0). \tag{5.14}$$

The sign of $F^{\mathrm{R}}(\rho)$ in the velocity equation depends on the direction of the rarefaction. A leftward rarefaction corresponds to the minus sign.

For shock waves, the pressure is given by

$$G^{\mathrm{S}}(\rho, \rho_0, p_0) = \frac{\left[A(\rho_0) + 0.5\left(\rho_0^{-1} - \rho^{-1}\right)\right] p_0 + B(\rho_0) - B(\rho)}{A(\rho) - 0.5(\rho_0^{-1} - \rho^{-1})}, \tag{5.15}$$

and velocity by

$$F^{\mathrm{S}}(\rho, \rho_0, p_0) = \sqrt{\left[G^{\mathrm{S}}(\rho, \rho_0, p_0) - p_0\right]\left[\rho_0^{-1} - \rho^{-1}\right]}. \tag{5.16}$$

5.1.2 Iteration with the Newton-Raphson method

The solution to the Riemann problem (equations (5.5) and (5.6)) is found iteratively. Since the wave jumps are functions of density, the densities on the left and right sides of the contact discontinuity are varied until a satisfactory solution is found. Here, the Newton-Raphson method is used to find the densities, $\boldsymbol{\rho} = (\rho_L^*, \rho_R^*)^T$, where ρ_L^* and ρ_R^* are the densities at the left and right sides of the contact discontinuity. Once the densities have been found, the pressures and velocities are found by application of the jump relations, i.e. the functions G^{R}, G^{S}, F^{R}, and F^{S}. The Newton-Raphson method iterates on the variables by

$$\boldsymbol{x}_{i+1} = \boldsymbol{x}_i - \mathbf{J}^{-1}(\boldsymbol{x})\mathbf{f}(\boldsymbol{x}_i), \tag{5.17}$$

where $\mathbf{f}(\boldsymbol{x})$ is the function for which a root is sought, $\mathbf{x}$ is the vector of variables the function depends on, $\mathbf{J}^{-1}(\boldsymbol{x})$ is the Jacobian of $\mathbf{f}$, and subscripts denotes the iteration number. The pressure and velocity equality over the contact discontinuity define the two equations that determine ρ_L^* and ρ_R^*. These can be written

$$f_1(\rho_L^*, \rho_R^*) = G_{\mathrm{L}}^{\mathrm{W}}(\rho_{\mathrm{L}}^*) - G_{\mathrm{R}}^{\mathrm{W}}(\rho_{\mathrm{R}}^*) = 0, \tag{5.18}$$

and

$$f_2(\rho_L^*, \rho_R^*) = u_{\mathrm{L}} - F_{\mathrm{L}}^{\mathrm{W}}(\rho_{\mathrm{L}}^*) - u_{\mathrm{R}} - F_{\mathrm{R}}^{\mathrm{W}}(\rho_{\mathrm{R}}^*) = 0, \tag{5.19}$$

where W = R if $\rho \leq \rho_0$ (rarefaction), W = S if $\rho > \rho_0$, and subscripts L, R indicates which values to insert for ρ_0 and p_0 in the jump relations. Then, $\mathbf{f}(\rho_L^*, \rho_R^*) = (f_1(\rho_L^*, \rho_R^*), f_2(\rho_L^*, \rho_R^*))^T$, and the inverse Jacobian is

$$\mathbf{J}^{-1} = \frac{1}{\left[a^{\mathrm{W}}(\rho_{\mathrm{L}}^*)d^{\mathrm{W}}(\rho_{\mathrm{R}}^*) - b^{\mathrm{W}}(\rho_{\mathrm{R}}^*)c^{\mathrm{W}}(\rho_{\mathrm{L}}^*)\right]} \begin{bmatrix} d^{\mathrm{W}}(\rho_{\mathrm{R}}^*) & -b^{\mathrm{W}}(\rho_{\mathrm{R}}^*) \\ -c^{\mathrm{W}}(\rho_{\mathrm{L}}^*) & a^{\mathrm{W}}(\rho_{\mathrm{L}}^*) \end{bmatrix}, \tag{5.20}$$

where again W = R if $\rho \leq \rho_0$ (rarefaction) and W = S if $\rho > \rho_0$, and

$$\begin{aligned} a(\rho_{\mathrm{L}}^*) &= \frac{dG_{\mathrm{L}}^{\mathrm{W}}(\rho_{\mathrm{L}}^*)}{d\rho_{\mathrm{L}}^*}, \quad b(\rho_{\mathrm{R}}^*) = -\frac{dG_{\mathrm{R}}^{\mathrm{W}}(\rho_{\mathrm{R}}^*)}{d\rho_{\mathrm{R}}^*}, \\ c(\rho_{\mathrm{L}}^*) &= -\frac{dF^{\mathrm{W}}(\rho_{\mathrm{L}}^*)}{d\rho_{\mathrm{L}}^*}, \quad d(\rho_{\mathrm{R}}^*) = -\frac{dF^{\mathrm{W}}(\rho_{\mathrm{R}}^*)}{d\rho_{\mathrm{R}}^*}. \end{aligned} \tag{5.21}$$

These functions are simple algebraic relations (Hennessey et al., 2020), given by

$$\frac{dG^{\mathrm{R}}(\rho)}{d\rho} = c^2, \tag{5.22}$$

$$\frac{dG^{\mathrm{S}}(\rho)}{d\rho} = \frac{A(\rho)c^2 - 0.5\rho^{-2}(G^{\mathrm{S}}(\rho) - p_0)}{A(\rho) - 0.5(\rho_0^{-1} - \rho^{-1})}, \tag{5.23}$$

$$\frac{dF^{\mathrm{R}}(\rho)}{d\rho} = \frac{c}{\rho}, \tag{5.24}$$

$$\frac{dF^{\mathrm{S}}(\rho)}{d\rho} = \frac{1}{2F^{\mathrm{S}}(\rho)}\left[\left(\rho_0^{-1} - \rho^{-1}\right)\frac{dG^{\mathrm{S}}(\rho)}{d\rho} + \rho^{-2}\left(G^{\mathrm{S}}(\rho) - p_0\right)\right]. \tag{5.25}$$

The iteration is stopped when the relative change in density becomes smaller than a chosen criterion.

5.1.3 Iteration with Brent's method

Some problems involving large density and pressure discontinuities are difficult for the Newton-Raphson method, and the method can take a long time to converge, or not converge at all. This is a problem for water-air configurations, especially in UNDEX events, since large pressure and density jumps are encountered simultaneously. An alternative solution procedure is to instead use Brent's method to solve equations (5.18) and (5.19). Brent's method is a univariate root finding method, and must therefore use nested iterations in order to solve both equations simultaneously.

To do this, one can first define an outer iteration that iterates over ρ_{L}^{*} to solve equation (5.19). Within each outer iteration, an inner iteration can be performed to solve equation (5.18) for ρ_{R}^{*}. Once the outer iteration converges, the solution is found. Brent's method has the advantage of guaranteed convergence, in contrast to the Newton-Raphson method, as long as bracketing intervals can be found for the zeros of equations (5.18) and (5.19). This makes Brent's method suitable for simulating underwater explosions, and is therefore used in the rest of this document. However, it is worth mentioning that if the Newton-Raphson method is provided an appropriate initial guess, it can be substantially more efficient than Brent's method.

5.2 Approximate flux-schemes

In this report, two different flux schemes are used in combination with the exact Riemann solver. These are the Harten-Lax-van Leer contact (HLLC) scheme (Toro et al., 1994), as well as a variant of the Lax-Friedrich scheme. The HLLC scheme is sufficiently described in Toro et al. (1994) and is therefore not written out here. The Lax-Friedrich scheme computes the fluxes as

$$F_{\rho} = \frac{u_L + u_R}{\rho_L^{-1} + \rho_R^{-1}} - \frac{1}{2}\left[\frac{1}{2}(c_L + c_R) + \frac{1}{2}\left|u_L + u_R\right|\right](\rho_R - \rho_L), \tag{5.26}$$

$$\begin{aligned} F_{\rho u} =& \frac{1}{2}\frac{(u_L + u_R)^2}{\rho_L^{-1} + \rho_R^{-1}} + \frac{1}{2}(p_L + p_R) - \frac{1}{4}\left[\frac{1}{2}(c_L + c_R) + \frac{1}{2}\left|u_L + u_R\right|\right](\rho_R - \rho_L)(u_L + u_R) \\ & -\frac{1}{4}\left[\frac{1}{2}(c_L + c_R) + \frac{1}{2}\left|u_L + u_R\right|\right](\rho_L + \rho_R)(u_R - u_L), \end{aligned} \tag{5.27}$$

$$\begin{aligned} F_{\rho E} =& \left(\frac{u_L + u_R}{\rho_L^{-1} + \rho_R^{-1}}\right)\frac{1}{2}(h_L + h_L + u_L u_R) \\ & - \frac{1}{2}\left[\frac{1}{2}(c_L + c_R) + \frac{1}{4}\left|u_L + u_R\right|\right](\rho_R - \rho_L)\frac{1}{2}(e_L + e_R + u_L u_R) \\ & - \frac{1}{4}\left[\frac{1}{2}(c_L + c_R) + \frac{1}{2}\left|u_L + u_R\right|\right](\rho_L + \rho_R)\left[e_R - e_L + (u_L + u_R)(u_R - u_L)\right], \end{aligned} \tag{5.28}$$

The input data to both flux schemes are the face-interpolated and limited primitive variables, which are computed with a MUSCL scheme. The minmod limiter is used unless otherwise specified.

5.3 FIVER algorithm

The description of the FIVER algorithm in Farhat et al. (2008) is written to accommodate both implicit schemes, predictor-corrector schemes as well as explicit time-stepping schemes. Only

explicit schemes will be used here, and the specific algorithm used here is described below. The algorithm is straightforward, and uses a standard RK4 integration scheme. In the following, $\mathbf{q}$ denotes the vector of conserved variables.

(1) Step the Euler equations forward in time with the RK4 scheme based on $\mathbf{q}(t_0)$ and $z(t_0)$ to obtain $\mathbf{q}(t_0 + \Delta t)$. In all sub-timesteps, evaluate the fluxes with the levelset function $z(t_0)$.

(1.1) For all faces where the sign of the levelset function is equal on both sides, compute the flux using the chosen single-fluid, approximate flux-scheme.

(1.2) For faces where the sign of the levelset function is different on the two sides, compute the solution of the exact Riemann problem. Use the part of the exact solution around the contact discontinuity to define two new Riemann problems, as shown in figure 3.2. For the left control volume, compute the flux using the interpolated and limited left face state and the state in the exact solution left of the contact discontinuity. Similarly, for the right control volume, use the exact solution to the right of the contact discontinuity and the interpolated and limited right face state. Use these sets of states to compute the flux with the same flux scheme as for the single-fluid faces.

(2) Step the levelset equation forward using the RK4 scheme to obtain $z(t_0 + \Delta t)$ using $\mathbf{q}(t_0 + \Delta t)$ and $z(t_0)$. In all sub-timesteps, evaluate the levelset flux using $\mathbf{q}(t_0 + \Delta t)$.

(3) For control volumes where the sign of the level-set function changes, i.e. where $z(\mathbf{x},\ t_0 + \Delta t)z(\mathbf{x},\ t_0) < 0$, replace $\mathbf{q}(\mathbf{x},\ t_0 + \Delta t)$ with the exact solution of the Riemann problem. As long as there is not an interface on multiple sides of the control-volume, this is unique, and the part of the exact solution to use can be identified based on the sign of the velocity. For multi-dimensional problems, multiple interface cases can happen, and in that case some averaging of the exact solutions must be used. Averaging methods for the multiple interface cases have been evaluated in Main et al. (2017).

6 Numerical tests

The following tests are conducted with a RK4 time integration scheme, MUSCL reconstruction with the minmod limiter and either a HLLC or Lax-Friedrich flux. Unless otherwise specified, the x direction is discretized into 100 control volumes between $x = 0$ m and $x = 1$ m, and the timestep controlled by a constant CFL-number of 0.9. Six test problems are considered here. These are summarized in table 6.1. The six problems cover a range of conditions and material properties, and serve as a comprehensive test of the numerical method for one-dimensional problems. In the following sections, the problems will be referred to by their name given in the first column of table 6.1.

Table 6.1 Setup of the numerical test problems, where $\rho_{L,R}$ are given in kg/m^3, $u_{L,R}$ are given in m/s and $p_{L,R}$ are given in Pa.

	Left material EOS	$(\rho_L, u_L, p_L)^T$	$(\rho_R, u_R, p_R)^T$	Right material EOS
Sod shock tube	IG $\gamma = 1.4$	$\begin{pmatrix} 1 \\ 0 \\ 1 \end{pmatrix}$	$\begin{pmatrix} 0.125 \\ 0 \\ 0.1 \end{pmatrix}$	IG $\gamma = 1.4$
Modified Sod	IG $\gamma = 1.4$	$\begin{pmatrix} 1 \\ 0 \\ 1 \end{pmatrix}$	$\begin{pmatrix} 0.125 \\ 0 \\ 0.1 \end{pmatrix}$	IG $\gamma = 1.6$
IG-SG Sod	IG $\gamma = 1.4$	$\begin{pmatrix} 1 \\ 0 \\ 1 \end{pmatrix}$	$\begin{pmatrix} 0.125 \\ 0 \\ 0.1 \end{pmatrix}$	SG $\gamma = 1.6$, $\pi = 0.2$
Blast wave	IG $\gamma = 1.4$	$\begin{pmatrix} 1 \\ 0 \\ 1000 \end{pmatrix}$	$\begin{pmatrix} 1 \\ 0 \\ 0.01 \end{pmatrix}$	IG $\gamma = 1.4$
Water-gas	SG $\gamma = 4.4$, $\pi = 6 \times 10^8$	$\begin{pmatrix} 1000 \\ 0 \\ 10^9 \end{pmatrix}$	$\begin{pmatrix} 50 \\ 0 \\ 10^5 \end{pmatrix}$	IG $\gamma = 1.4$
LX-17	JWL $A = 6.321 \times 10^{13}$, $B = -4.472 \times 10^9$, $R_1 = 11.3$, $R_2 = 1.13$, $\omega = 0.8938$, $\rho_0 = 1905$, $e_0 = 0$	$\begin{pmatrix} 952.5 \\ 0 \\ 10^{11} \end{pmatrix}$	$\begin{pmatrix} 3810 \\ 0 \\ 2 \times 10^{11} \end{pmatrix}$	JWL $A = 6.321 \times 10^{13}$, $B = -4.472 \times 10^9$, $R_1 = 11.3$, $R_2 = 1.13$, $\omega = 0.8938$, $\rho_0 = 1905$, $e_0 = 0$
TNT-water	JWL $A = 3.712 \times 10^{11}$, $B = 3.230 \times 10^9$, $R_1 = 4.15$, $R_2 = 0.95$, $\omega = 0.3$, $\rho_0 = 1630$ $e_0 = 0$	$\begin{pmatrix} 1630 \\ 0 \\ 8.318 \times 10^9 \end{pmatrix}$	$\begin{pmatrix} 1025 \\ 0 \\ 10^6 \end{pmatrix}$	SG $\gamma = 7.1$, $\pi = 3.309 \times 10^8$

6.1 Sod's shock tube

The standard Sod shock tube test is shown in figure 6.1. The numerical results agree well with the exact solution, and the strength and position of the various waves are well captured.

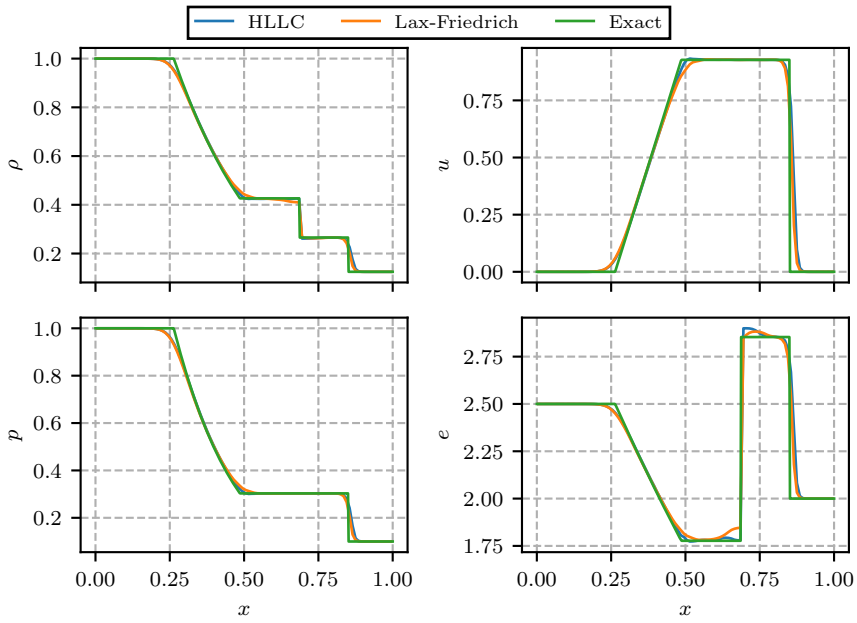

Figure 6.1 Sod shock tube problem at $t = 0.2$ s.

6.2 Modified Sod problem

A modified version of Sod's shock tube problem was considered in Abgrall and Karni (2001) and Farhat et al. (2008), where the equation of state of the gas on the right side is set to an ideal gas with $\gamma = 1.6$. The conditions and material properties are given in table 6.1 as the "modified Sod" problem. The numerical results and the exact solution for this problem is shown in figure 6.2

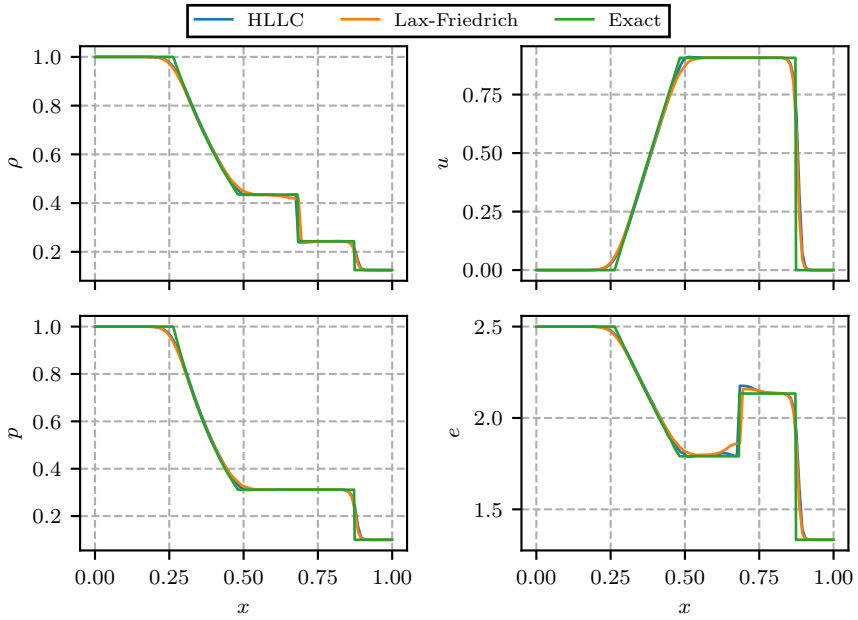

Figure 6.2 Modified Sod shock tube problem at $t = 0.2$ s, where the gas on the right side is an ideal gas with $\gamma = 1.6$.

6.3 Ideal gas - Stiffened gas Sod problem

Next, initial conditions similar to Sod's shock tube are considered, but with a stiffened gas (SG) on the right side. The initial conditions and material properties are reported in table 6.1 as the "IG-SG Sod" problem. The results, along with the exact solution are shown in figure 6.3.

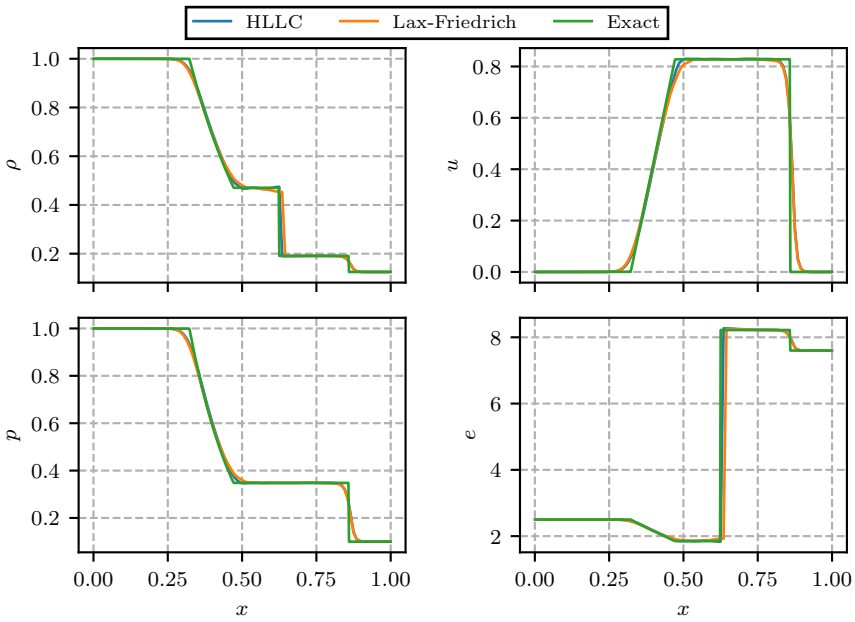

Figure 6.3 IG-SG Sod shock tube problem at $t = 0.15$ s.

6.4 Blast wave problem

The blast wave problem (test 4 for the exact Riemann solver in Toro (2013)) is shown in figure 6.4. This problem features a strong pressure jump (a factor 10^6) with initially equal densities in the left and right states, and the material is also the same at both sides. For this problem the domain is discretized into 400 volumes. Apart from a minor disturbance at the tail of the rarefaction wave, the exact solution is well reproduced for both flux schemes.

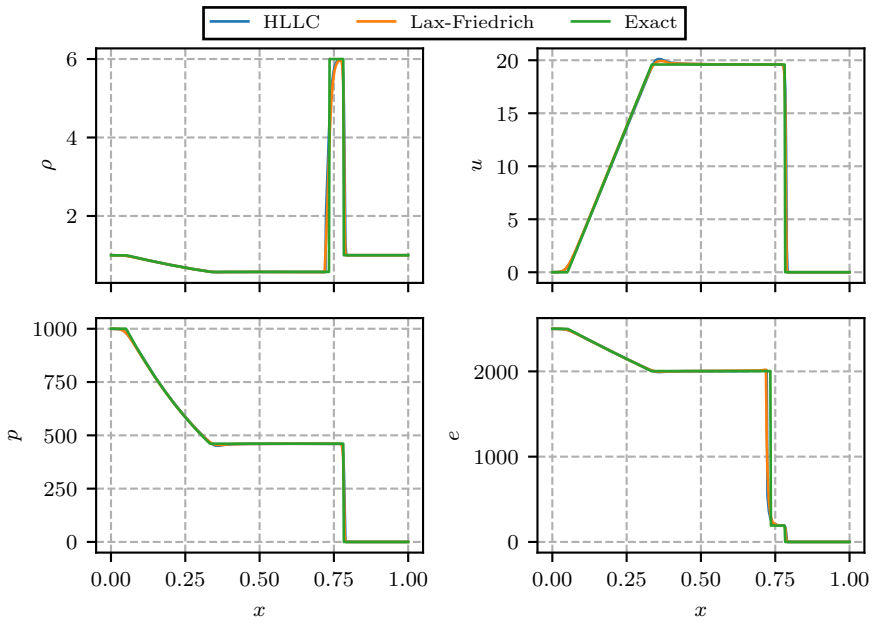

Figure 6.4 Blast wave problem (Toro test problem 4) at $t = 0.012$. s

6.5 Water - gas problem

Farhat et al. (2008) considered a shock tube problem resembling the interaction between water and an ideal gas. The initial conditions and material parameters are given in table 6.1 in the "Water-gas" row. For this problem, the discontinuity is located at $x = 0.7$ m. The results are shown at $t = 2.4 \times 10^{-4}$ s with a spatial resolution of $\Delta x = 1/200$ m in figure 6.5 and with $\Delta x = 1/800$ m in figure 6.6. Note that the positions of both the shock wave and the material contact are slightly off. The solution presented in Farhat et al. (2008) is at the correct location. Since the main difference between the methods here and in Farhat et al. (2008) are the flux schemes, it can be hypothesized that the shock position discrepancy is a result of using the Lax-Friedrich or HLLC fluxes instead of the Roe flux. Note however, that the strength of the shock and contact wave is correct for both flux schemes.

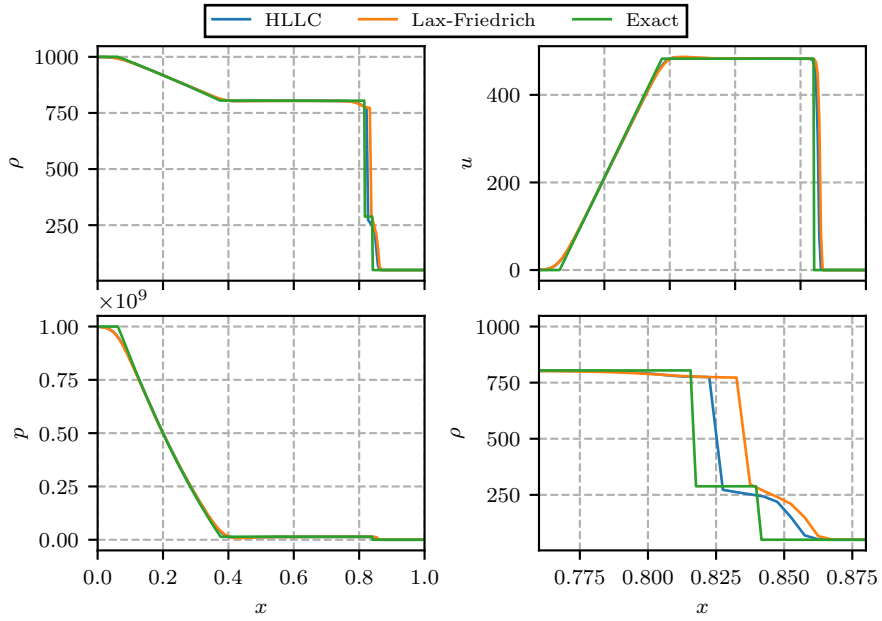

Figure 6.5 Water-gas bubble problem at $t = 2.4 \times 10^{-4}$ s with $\Delta x = 1/200$ m.

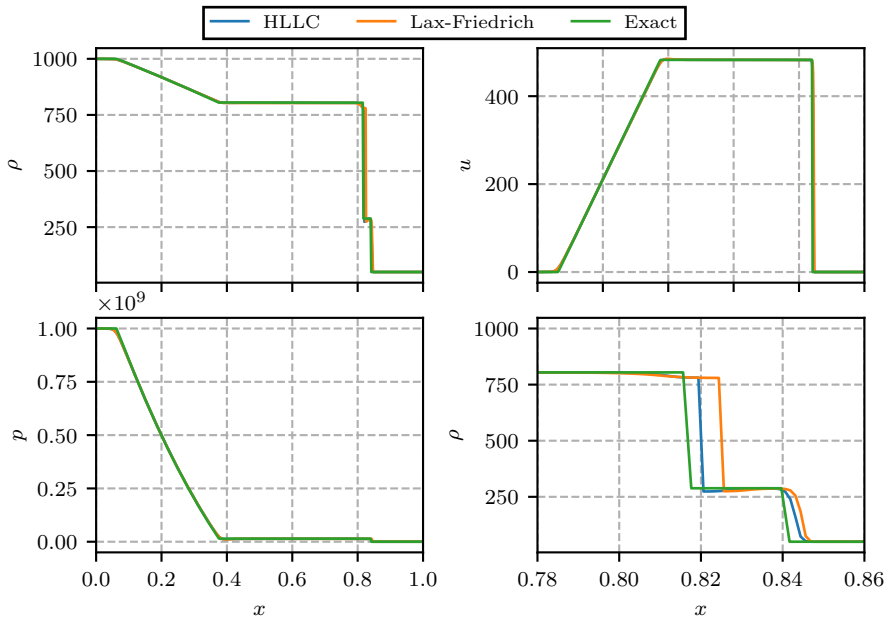

Figure 6.6 Water-gas bubble problem at $t = 2.4 \times 10^{-4}$ *s with* $\Delta x = 1/800$ *m.*

6.6 LX-17 problem

Banks (2010); Lee et al. (2013); Price et al. (2015) considered a single-material shock tube with LX-17 explosive in two states. The LX-17 material is modeled with a JWL equation of state. The initial conditions and material parameters are given in table 6.1 in the LX-17 row. The exact solution and the numerical results at $t = 2 \times 10^{-5}$ s are shown in figure 6.7. Again, there is a slight error in the position of the material interface, but otherwise the solution is accurately captured by the numerical method.

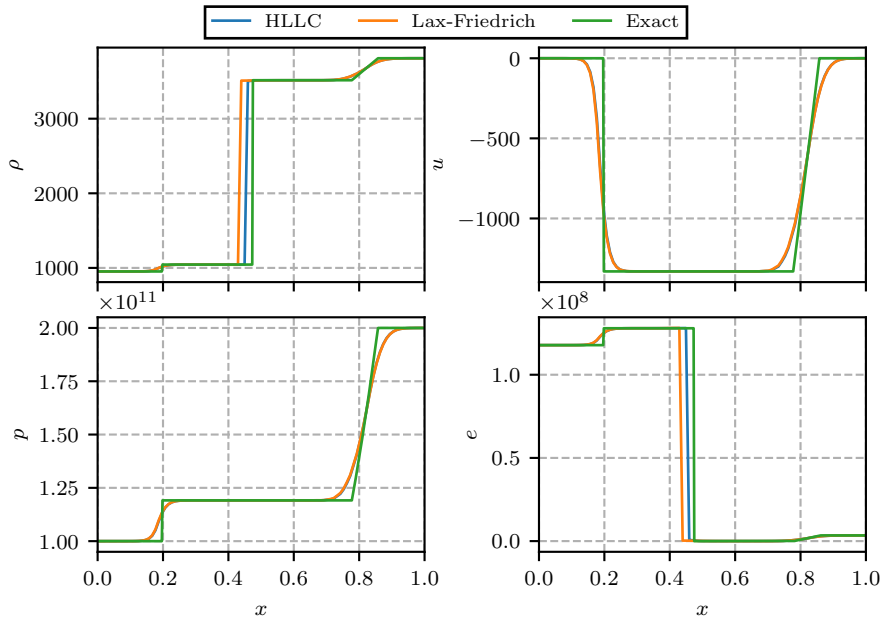

Figure 6.7 LX-17 shock tube problem at $t = 2 \times 10^{-5}$ s with $\Delta x = 1/100$ m.

6.7 TNT-water problem

This problem features an expanding bubble of TNT detonation product gases in water. This is similar to the spherically symmetric problem considered in Farhat et al. (2012). The material properties and initial conditions are given in table 6.1 under the TNT-water row. The exact solution and the numerical results at $t = 10^{-4}$ s are shown in figure 6.8.

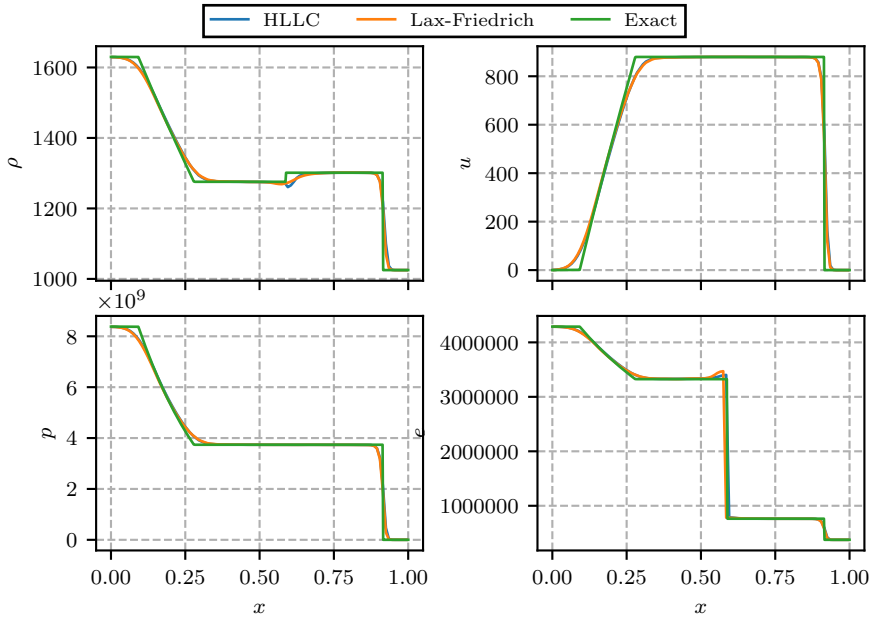

Figure 6.8 TNT-water problem at $t = 10^{-4}$ s with $\Delta x = 1/100$ m.

7 Conclusions

Understanding of underwater explosion phenomena is important for design and operation of offshore/subsea installations and ships. UNDEX event simulations can provide high-resolution data in space and time for any parameter of interest, such as pressure fields, bulk-cavitation regions etc. However, the multi-phase flow in an UNDEX event is a challenging multi-physics problem which can not readily be simulated with most computational fluid dynamics software today.

This report has discussed the key components of an UNDEX event. Empirical models commonly used for limited parts of UNDEX events were introduced. Empirical models can be useful for design and operation, but they cannot improve the understanding of UNDEX events. Instead, this requires accurate simulation capabilities. Several models for simulation of underwater explosions have been reviewed, and strengths and weaknesses for the models were discussed. The ability of the model to retain and track a sharp gas-water interface over long periods of time is of particular importance. The "finite volume method with exact two-phase Riemann solver" (FIVER) was found most suitable for the problems of interest in FFI project 1447. This method was implemented in the CFD software Charles.

The implementation was verified with the aid of test problems commonly used in the literature. The test problems also demonstrate FIVER's suitability for different conditions relevant to underwater explosion events. The tests consist of one-dimensional problems with a wide range of pressure, density, and velocity jumps, as well as several equations of state. Overall, the model performs well for all the test problems, but in some cases, the location of the material interface is slightly offset from its location in the exact Riemann problem solution. The choice of approximate flux scheme was shown to affect this error.

The model was found to be suitable for simulation of underwater explosions. Future work will implement the model in multiple dimensions, and apply it to underwater explosion scenarios. Additionally, the code will be coupled to a structure response code to simulate the response of ships to underwater explosions.

References

Abgrall, R. and Karni, S. (2001). Computations of compressible multifluids. *Journal of Computational Physics*, 169(2):594–623.

Allaire, G., Clerc, S., and Kokh, S. (2002). A five-equation model for the simulation of interfaces between compressible fluids. *Journal of Computational Physics*, 181(2):577–616.

Ball, G. J., Howell, B. P., Leighton, T. G., and Schofield, M. J. (2000). Shock-induced collapse of a cylindrical air cavity in water: a free-Lagrange simulation. *Shock Waves*, 10(4):265–276.

Banks, J. W. (2010). On exact conservation for the Euler equations with complex equations of state. *Communications in Computational Physics*, 8(5):995.

Blake, J. R., Taib, B. B., and Doherty, G. (1986). Transient cavities near boundaries. Part 1. Rigid boundary. *Journal of Fluid Mechanics*, 170:479–497.

Chandran, J. and Salih, A. (2019). A modified equation of state for water for a wide range of pressure and the concept of water shock tube. *Fluid Phase Equilibria*, 483:182–188.

Cole, R. H. (1948). *Underwater explosions*. Princeton university press.

Costanzo, F. A. (2011). Underwater explosion phenomena and shock physics. In *Structural Dynamics, Volume 3*, pages 917–938. Springer.

Farhat, C., Gerbeau, J.-F., and Rallu, A. (2012). FIVER: A finite volume method based on exact two-phase Riemann problems and sparse grids for multi-material flows with large density jumps. *Journal of Computational Physics*, 231(19):6360–6379.

Farhat, C., Rallu, A., and Shankaran, S. (2008). A higher-order generalized ghost fluid method for the poor for the three-dimensional two-phase flow computation of underwater implosions. *Journal of Computational Physics*, 227(16):7674–7700.

Fedkiw, R. P., Aslam, T., Merriman, B., Osher, S., et al. (1999). A non-oscillatory Eulerian approach to interfaces in multimaterial flows (the ghost fluid method). *Journal of Computational Physics*, 152(2):457–492.

Gilmore, F. R. (1952). The growth or collapse of a spherical bubble in a viscous compressible liquid.

Hennessey, M., Kapila, A. K., and Schwendeman, D. W. (2020). An HLLC-type Riemann solver and high-resolution Godunov method for a two-phase model of reactive flow with general equations of state. *Journal of Computational Physics*, 405:109180.

Holt, M. (1977). Underwater explosions. *Annual Review of Fluid Mechanics*, 9(1):187–214.

Huang, Y. C., Hammitt, F. G., and Mitchell, T. M. (1973). Note on shock-wave velocity in high-speed liquid-solid impact. *Journal of Applied Physics*, 44(4):1868–1869.

Johnsen, E. and Colonius, T. (2009). Numerical simulations of non-spherical bubble collapse. *Journal of Fluid mechanics*, 629:231–262.

Kapila, A. K., Menikoff, R., Bdzil, J. B., Son, S. F., and Stewart, D. S. (2001). Two-phase modeling of deflagration-to-detonation transition in granular materials: Reduced equations. *Physics of Fluids*, 13(10):3002–3024.

Keller, J. B. and Miksis, M. (1980). Bubble oscillations of large amplitude. *The Journal of the Acoustical Society of America*, 68(2):628–633.

Kiran, J. H. (2016). Undervannsdetonasjoner - en kort innføring (in Norwegian). Technical Report 16/01500, Norwegian Defence Research Establishment (FFI).

Klaseboer, E., Hung, K. C., Wang, C., Wang, C., Khoo, B. C., Boyce, P., Debono, S., and Charlier, H. (2005). Experimental and numerical investigation of the dynamics of an underwater explosion bubble near a resilient/rigid structure. *Journal of Fluid Mechanics*, 537:387–413.

Lee, B. J., Toro, E. F., Castro, C. E., and Nikiforakis, N. (2013). Adaptive Osher-type scheme for the Euler equations with highly nonlinear equations of state. *Journal of Computational Physics*, 246:165–183.

Li, T., Wang, S., Li, S., and Zhang, A.-M. (2018). Numerical investigation of an underwater explosion bubble based on FVM and VOF. *Applied Ocean Research*, 74:49–58.

Liu, T. G., Khoo, B. C., and Yeo, K. S. (2003). Ghost fluid method for strong shock impacting on material interface. *Journal of Computational Physics*, 190(2):651–681.

Liu, Y. L., Zhang, A. M., Tian, Z. L., and Wang, P. (2018). Numerical investigation on global responses of surface ship subjected to underwater explosion in waves. *Ocean Engineering*, 161:277–290.

Lozano, E., Jackson, G. S., and Petr, V. (2020). An Eulerian multimaterial framework for simulating high-explosive aquarium tests. *Computers & Fluids*, page 104524.

Main, A. and Farhat, C. (2014). A second-order time-accurate implicit finite volume method with exact two-phase Riemann problems for compressible multi-phase fluid and fluid–structure problems. *Journal of Computational Physics*, 258:613–633.

Main, A., Zeng, X., Avery, P., and Farhat, C. (2017). An enhanced FIVER method for multi-material flow problems with second-order convergence rate. *Journal of Computational Physics*, 329:141–172.

Park, J. (2019). Application of the Runge Kutta discontinuous Galerkin-direct ghost fluid method to internal explosion inside a water-filled tube. *International Journal of Naval Architecture and Ocean Engineering*, 11(1):572–583.

Pishevar, A. R. and Amirifar, R. (2010). An adaptive ALE method for underwater explosion simulations including cavitation. *Shock Waves*, 20(5):425–439.

Price, M. A., Nguyen, V.-T., Hassan, O., and Morgan, K. (2015). A method for compressible multimaterial flows with condensed phase explosive detonation and airblast on unstructured grids. *Computers & Fluids*, 111:76–90.

Rosseland, S. (1950). Underwater explosion research. Technical Report S-RF 67, Norwegian Defence Research Establishment.

Saurel, R., Petitpas, F., and Berry, R. A. (2009). Simple and efficient relaxation methods for interfaces separating compressible fluids, cavitating flows and shocks in multiphase mixtures. *Journal of Computational Physics*, 228(5):1678–1712.

Schmidmayer, K., Bryngelson, S. H., and Colonius, T. (2020). An assessment of multicomponent flow models and interface capturing schemes for spherical bubble dynamics. *Journal of Computational Physics*, 402:109080.

Terashima, H. and Tryggvason, G. (2009). A front-tracking/ghost-fluid method for fluid interfaces in compressible flows. *Journal of Computational Physics*, 228(11):4012–4037.

Toro, E. F. (2013). *Riemann solvers and numerical methods for fluid dynamics: a practical introduction*. Springer Science & Business Media.

Toro, E. F., Spruce, M., and Speares, W. (1994). Restoration of the contact surface in the HLL-Riemann solver. *Shock waves*, 4(1):25–34.

Turangan, C. K., Jamaluddin, A. R., Ball, G. J., and Leighton, T. G. (2008). Free-Lagrange simulations of the expansion and jetting collapse of air bubbles in water. *Journal of Fluid Mechanics*, 598:1–25.

Wang, G., Zhang, S., Yu, M., Li, H., and Kong, Y. (2014). Investigation of the shock wave propagation characteristics and cavitation effects of underwater explosion near boundaries. *Applied Ocean Research*, 46:40–53.

Wang, K. G. (2017). Multiphase fluid-solid coupled analysis of shock-bubble-stone interaction in shockwave lithotripsy. *International Journal for Numerical Methods in Biomedical Engineering*, 33(10):e2855.

Xie, W. F., Liu, T. G., and Khoo, B. C. (2007). The simulation of cavitating flows induced by underwater shock and free surface interaction. *Applied Numerical Mathematics*, 57(5-7):734–745.

About FFI

The Norwegian Defence Research Establishment (FFI) was founded 11th of April 1946. It is organised as an administrative agency subordinate to the Ministry of Defence.

FFI's mission

FFI is the prime institution responsible for defence related research in Norway. Its principal mission is to carry out research and development to meet the requirements of the Armed Forces. FFI has the role of chief adviser to the political and military leadership. In particular, the institute shall focus on aspects of the development in science and technology that can influence our security policy or defence planning.

FFI's vision

FFI turns knowledge and ideas into an efficient defence.

FFI's characteristics

Creative, daring, broad-minded and responsible.

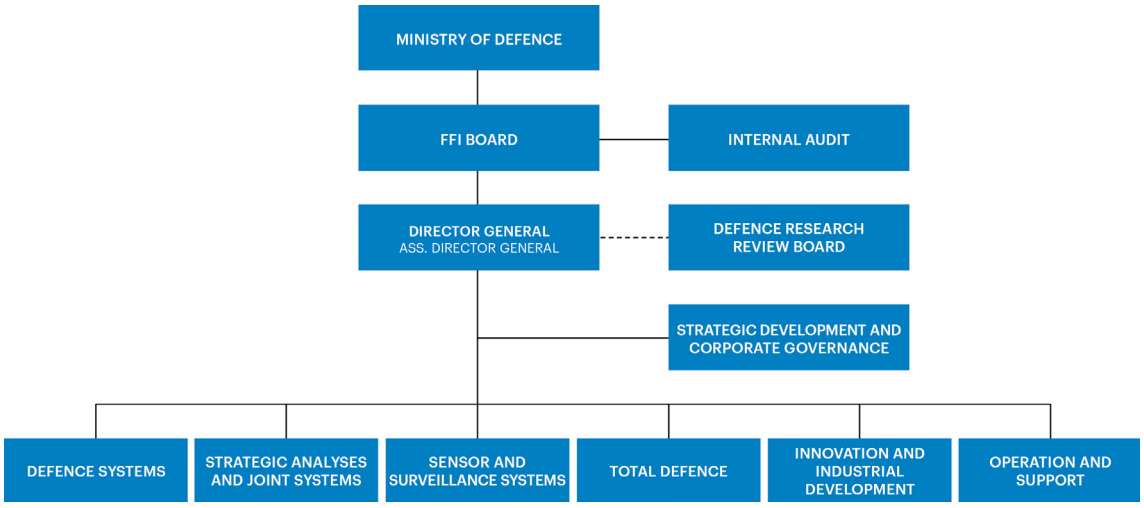

Forsvarets forskningsinstitutt
Postboks 25
2027 Kjeller

Besøksadresse:
Instituttveien 20
2007 Kjeller

Telefon: 63 80 70 00
Telefaks: 63 80 71 15
Epost: post@ffi.no

Norwegian Defence Research Establishment (FFI)
P.O. Box 25
NO-2027 Kjeller

Office address:
Instituttveien 20
N-2007 Kjeller

Telephone: +47 63 80 70 00
Telefax: +47 63 80 71 15
Email: post@ffi.no